

Integrable atomtronic interferometry

D.S. Grun¹, L.H. Ymai², K Wittmann W.¹, A.P. Tonel², A. Foerster¹, J. Links³

¹ Instituto de Física da UFRGS, Avenida Bento Gonçalves 9500, Porto Alegre, Rio Grande do Sul, Brazil,

² Universidade Federal do Pampa, Av. Maria Anunciação Gomes de Godoy 1650, Bag, Rio Grande do Sul, Brazil, and

³ School of Mathematics and Physics, The University of Queensland, Brisbane, Queensland, Australia.

(Dated: February 16, 2021)

High sensitivity quantum interferometry requires more than just access to entangled states. It is achieved through deep understanding of quantum correlations in a system. Integrable models offer the framework to develop this understanding. We communicate the design of interferometric protocols for an integrable model that describes the interaction of bosons in a four-site configuration. Analytic formulae for the quantum dynamics of certain observables are computed. These expose the system's functionality as both an interferometric identifier, and producer, of NOON states. Being equivalent to a controlled-phase gate acting on two hybrid qudits, this system also highlights an equivalence between Heisenberg-limited interferometry and quantum information. These results are expected to open new avenues for integrability-enhanced atomtronic technologies.

Introduction.— Recent developments in the manipulation of wave-like properties in matter are driving a raft of atom-interferometric applications, in the vicinity of the Heisenberg limit, within the field of quantum metrology [1, 2]. It has long been recognized that the ability to effectively and efficiently harness quantum interference is equivalent to implementing certain tasks in quantum computation [3]. Nowadays, ultracold quantum gases are proving to be successful in enabling quantum simulations, for phenomena such as quantum magnetism and topological states of matter, beyond the capabilities of classical supercomputers [4]. Through a confluence of these types of investigations, there are several efforts to push research towards designs for atomtronic devices [5–7], based on circuits with atomic currents. These devices promise high levels of control in the manipulation of many-body systems, leading to advanced sensitivity in metrology [8] and other quantum technologies [9–13].

Around a decade ago [14] a class of models was identified for physical realization of an interferometer, using dipolar atoms. The Hamiltonian governing the time evolution of the system is a generalized Bose-Hubbard model on four sites, with closed boundary conditions and long-ranged interactions. We begin by pinpointing a set of *integrable* couplings for the Hamiltonian. That is, choices of parameters for which there are four conserved operators, equal to the number of degrees of freedom. The property of integrability has two significant impacts: (i) integrable systems have unique properties, such as Poisson distribution in energy level statistics [15], absence of chaotic behaviors [16], and non-standard thermal equilibration [17]. The quantum Newton cradle [18] provided experimental verification of the latter; (ii) mathematically, integrability facilitates tractable, closed-form formulae to describe the physics.

In our study we utilize the conserved operators of the integrable system to guide the design of measurement protocols for interferometric tasks (see Fig. 1). Our results are applicable in a particular regime, designated as *resonant tunneling*, whereby the energy levels separate into distinct bands. Through an effective Hamilto-

nian approach, the entire energy spectrum and structure of eigenstates becomes explicit for resonant tunneling. Moreover, the behavior system is clear in quantum information theoretic terms. The interferometer is equivalent to a system of two *hybrid qudits* [19], and the time-evolution of states is equivalent to the operation of a *controlled-phase* gate [20, 21]. We describe proof of principle examples of high-fidelity measurement protocols to identify and produce certain NOON states [1, 3, 22–24].

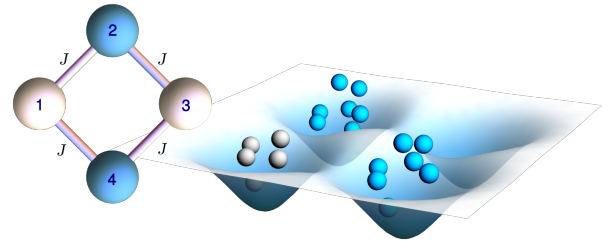


FIG. 1. Schematic representation of the interferometric circuit with tunneling between nearest neighbors. An initial state is prepared with M particles in site 1, and P particles in a (generally entangled) state across sites 2 and 4. After Hamiltonian time-evolution, measurement of particle number at site 3 is used to deduce information about the initial, or post-measurement, state across sites 2 and 4.

The model.— An extended Bose-Hubbard Hamiltonian on a square plaquette has the form [25, 26]

$$H = \frac{U_0}{2} \sum_{i=1}^4 N_i(N_i - 1) + \sum_{i=1}^4 \sum_{j=1, j \neq i}^4 \frac{U_{ij}}{2} N_i N_j - \frac{J}{2} [(a_1^\dagger + a_3^\dagger)(a_2 + a_4) + (a_2^\dagger + a_4^\dagger)(a_1 + a_3)]. \quad (1)$$

where $\{a_j, a_j^\dagger : j = 1, 2, 3, 4\}$ are canonical boson annihilation and creation operators, U_0 characterizes the short-range interactions between bosons at the same site, $U_{ij} = U_{ji}$ accounts for long-range (e.g. dipole-dipole) interactions between sites, and J represents the tun-

neling strength between neighboring sites. The Hamiltonian commutes with the total particle number $N = N_1 + N_2 + N_3 + N_4$ where $N_j = a_j^\dagger a_j$. Moreover, the Hamiltonian is integrable when $U_{13} = U_{24} = U_0$ and $U_{12} = U_{14} = U_{23} = U_{34}$. It acquires two additional conserved operators

$$Q_1 = \frac{1}{2}(N_1 + N_3 - a_1^\dagger a_3 - a_3^\dagger a_1),$$

$$Q_2 = \frac{1}{2}(N_2 + N_4 - a_2^\dagger a_4 - a_4^\dagger a_2),$$

such that $[Q_1, Q_2] = [Q_j, H] = [Q_j, N] = 0$, $j = 1, 2$. Integrability results from derivation of the model through the Quantum Inverse Scattering Method. It is intimately related to exact solvability, due to the algebraic Bethe Ansatz [27]. Hereafter we only consider the integrable case.

Resonant tunneling regime.— It is straightforward to check that there are large energy degeneracies when $J = 0$. From numerical diagonalization of (1), with N particles and sufficiently small value of J , it is seen that the low-energy levels coalesce into well-defined bands, similar to that observed in an analogous integrable three-site model [10, 28]. In this regime, an effective Hamiltonian H_{eff} is obtained through consideration of second-order tunneling processes. For an initial Fock state $|M-l, P-k, l, k\rangle$, with total boson number $N = M + P$, the effective Hamiltonian is a simple function of the conserved operators

$$H_{\text{eff}} = (N + 1)\Omega(Q_1 + Q_2) - 2\Omega Q_1 Q_2, \quad (2)$$

where $\Omega = J^2/(4U((M-P)^2 - 1))$ with $U = (U_{12} - U_0)/4$. This result is valid for $J \ll U(M-P)$, which characterizes the resonant tunneling regime. For time evolution under H_{eff} , both $N_1 + N_3 = M$ and $N_2 + N_4 = P$ are constant. The respective $(M+1)$ -dimensional subspace associated with sites 1 and 3 and $(P+1)$ -dimensional subspace associated with sites 2 and 4 serve as two, coupled, hybrid qudits [19], and provide the state space for the relevant energy band (see Appendix A). This yields a robust approximation for the dynamics under (1), which we benchmark below. For later use we will designate the qudit associated with sites 1 and 3 as *qudit A*, and that associated with sites 2 and 4 as *qudit B*.

It is easily found, through Bogoliubov transformations, that the spectrum of H_{eff} is simply

$$E_{\text{eff}} = (N + 1)\Omega(q_1 + q_2) - 2\Omega q_1 q_2$$

with $q_1 = 0, \dots, M$ and $q_2 = 0, \dots, P$. Thus the time evolution under H_{eff} is recognized as a controlled-phase gate [20, 21]. From here, several analytic results are accessible. For initial Fock state $|M, P, 0, 0\rangle$ it is found that the expectation value of the number imbalance between sites 1 and 3 is (in units where $\hbar = 1$)

$$\langle N_1 - N_3 \rangle = M \cos((M+1)\Omega t) [\cos(\Omega t)]^P \quad (3)$$

When $P = 0$, there are harmonic oscillations in the imbalance. For non-zero P , interference leads to a collapse and revival of oscillations. For comparison, results from numerical diagonalization of (1) are shown in the upper panels of Fig. 2

Other initial states can be studied, such as

$$|\Phi(\phi)\rangle = \frac{1}{\sqrt{2}} |M, P, 0, 0\rangle + \frac{\exp(i\phi)}{\sqrt{2}} |M, 0, 0, P\rangle, \quad (4)$$

which is a product of a number state for site 1, vacuum for site 3 (qudit A), and a phase-dependent NOON state [1, 3] across sites 2 and 4 (qudit B). We find the following result for the imbalance between sites 1 and 3:

$$\langle N_1 - N_3 \rangle = M \cos((M+1)\Omega t) [\cos(\Omega t)]^P + M \cos(\phi) \cos((M+1)\Omega t + \pi P/2) [\sin(\Omega t)]^P. \quad (5)$$

This formula provides excellent agreement with numerical calculations using (1). Illustrative examples are provided, for choices $\phi = 0$ and $\phi = \pi$, in the lower panels of Fig. 2.

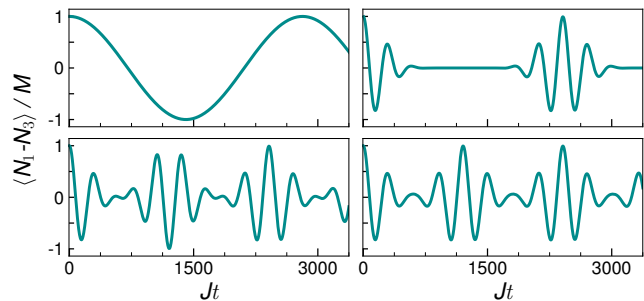


FIG. 2. Time evolution of expected fractional imbalance $\langle N_1 - N_3 \rangle / M$ for the Hamiltonian (1) as a function of dimensionless time Jt , with $U/J = 8$ and different initial states. Upper panels: Left: $|15, 0, 0, 0\rangle$. Right: $|15, 10, 0, 0\rangle$. Bottom panels: $(|15, 10, 0, 0\rangle + \exp(i\phi)|15, 0, 0, 10\rangle)/\sqrt{2}$ with $\phi = 0$ on the left and $\phi = \pi$ on the right. The top panels display agreement with the formula (3), while the bottom panels are in agreement with (5).

NOON state identification and production.— The above results are sufficient to demonstrate the efficacy of the system to perform certain interferometric tasks. First consider a black box processor \mathbb{P} that outputs one of two possible NOON states, either symmetric or anti-symmetric. The output state, with particle number P , is loaded into qudit B. With M particles in site 1 and zero in site 3 of qudit A, this composite initial state is given by (4) with either $\phi = 0$ (symmetric) or $\phi = \pi$ (anti-symmetric). Choose M such that $N = M + P$ is odd, let the system evolve for time $t_m = \pi/(2\Omega)$, and then measure the particle number at site 3. According to (5), there are only two possible measurement outcomes. One is to obtain the outcome zero, which occurs with probability 1 when $\phi = \pi$. The other is to obtain the outcome M , which occurs with probability 1 when $\phi = 0$ (cf. the

lower panels of Fig. 2, where the time of measurement is $t_m \approx 1206.37/J$. Moreover, this measurement is non-destructive and the NOON state in qudit B is preserved. See Appendix B for details.

This analytic result is an excellent approximation for the behavior governed by (1). From numerical results using the parameters of Fig. 2, we find that the success probability when $\phi = 0$ is 0.98699, and it is 0.98708 when $\phi = \pi$. This delivers a proof of principle example to show that the model (1) has capacity to perform interferometry with high accuracy.

One of the counter-intuitive features of this theoretical framework is the acute dependence on whether the total particle number $N = M + P$ is even or odd. To provide an understanding of this phenomenon, we take the initial state $|M, P, 0, 0\rangle$ and consider the time evolution of the *reduced density matrix* $\rho_{1,3}(t)$ for qudit A

$$\rho_{1,3}(t) = \text{tr}_{2,4}(|\Psi(t)\rangle\langle\Psi(t)|)$$

where $\text{tr}_{2,4}$ is the partial trace taken over the state space for qudit B, and $|\Psi(t)\rangle = \exp(-itH_{\text{eff}})|M, P, 0, 0\rangle$. We then obtain

$$\rho_{1,3}(t_m) = \frac{1}{2}|\Psi_+\rangle\langle\Psi_+| + \frac{1}{2}|\Psi_-\rangle\langle\Psi_-| \quad (6)$$

where

$$|\Psi_{\pm}\rangle = \frac{1}{\sqrt{2^M}} \sum_{r=0}^M \sqrt{\binom{M}{r}} \exp\left(-i\frac{(N \pm 1)r\pi}{2}\right) |\chi(r)\rangle,$$

$$|\chi(r)\rangle = \frac{1}{\sqrt{2^M(M-r)!r!}} (a_1^\dagger + a_3^\dagger)^{M-r} (a_1^\dagger - a_3^\dagger)^r |0\rangle.$$

The above results then allow for a calculation of the probability $\mathcal{P}(r)$ that, measurement of the number of particles at site 3, when $t = t_m$, yields the outcome r . The result is

$$\mathcal{P}(r) = \frac{1}{2}b_{M,r}(\sin^2((N-1)\pi/4)) + \frac{1}{2}b_{M,r}(\sin^2((N+1)\pi/4))$$

where $b_{M,r}(x) = \binom{M}{r} x^r (1-x)^{M-r}$, $r = 1, \dots, M$, are the *Bernstein polynomials*. When N is even,

$$\mathcal{P}(r) = \frac{1}{2^M} \binom{M}{r}.$$

When N is odd,

$$\mathcal{P}(r) = \frac{1}{2}\delta_{r,0} + \frac{1}{2}\delta_{r,M}. \quad (7)$$

The binomial distribution of the even case has maximal support, in stark contrast to the double delta function distribution of the odd case.

Remarkably, the earlier analysis on NOON state identification can now be inverted to show that the interferometer itself provides a high-fidelity simulation of the black box processor \mathbb{P} . For odd N it can be shown that

$$|\Psi(t_m)\rangle = \frac{(-1)^{(N+1)/2}}{2} |M, P, 0, 0\rangle + \frac{1}{2} |M, 0, 0, P\rangle + \frac{1}{2} |0, P, M, 0\rangle + \frac{(-1)^{(N-1)/2}}{2} |0, 0, M, P\rangle. \quad (8)$$

In accordance with the previous discussion, measurement at site 3 produces one of only two possible outcomes. A measurement outcome of M causes wavefunction collapse such that the state of qudit B is the symmetric (anti-symmetric) NOON state if $(N+1)/2$ is odd (even). Conversely, a measurement outcome of zero causes wavefunction collapse with an anti-symmetric (symmetric) NOON state in qudit B if $(N+1)/2$ is odd (even).

As before, it is useful to compare this result obtained from (2) against the analogous predictions of (1). Numerically, using the parameters of Fig. 2, we find that the outcome fidelity of this processor simulation for (1) is 0.99605 for outcome zero, and 0.99959 for outcome M , with respective probabilities of 0.497463 and 0.493898, close to the predictions of Eq. (7). Probabilities and fidelities for intermediate outcomes are provided in Appendix C.

Entanglement.— The ability to produce NOON states as described above is clearly dependent on the ability to create entanglement. More important is the ability to create “useful” entanglement since, as emphasized in the review article [1]: “Not all entangled states are useful for quantum metrology”. See also [29]. Below we demonstrate how this notion applies in the present context.

It is convenient for our study to use the entanglement measure of *linear entropy* defined in terms of a density matrix ρ as [30, 31]

$$\mathcal{E}(\rho) = 1 - \text{tr}(\rho^2).$$

The linear entropy is bounded between 0 and $1 - 1/d$, where d is the dimension of the space on which the density matrix acts. It follows from (6) that $\mathcal{E}(\rho_{1,3}(t_m)) = 1/2$. This result is independent of P . It asserts that immediately prior to making measurement at site 3, at time $t = t_m$, the entanglement between qudits A and B is *independent* of whether $N = M + P$ is even or odd.

Further, let $\rho_3(t_m) = \text{tr}_1(\rho_{1,3}(t_m))$, which can be expressed compactly as

$$\rho_3(t_m) = \sum_{q=0}^M \mathcal{P}(q) |q\rangle\langle q|.$$

The linear entropy of ρ_3 quantifies the entanglement between the subsystems, sites 1 and 3, within qudit A. Now we encounter a difference between the even and odd

cases. When N is odd, $\mathcal{E}(\rho_3(t_m)) = 1/2$. For even N

$$\begin{aligned}\mathcal{E}(\rho_3(t_m)) &= 1 - \frac{1}{2^{2M}} \binom{2M}{M} \\ &\sim 1 - \frac{1}{\sqrt{M\pi}}\end{aligned}$$

where the second step invokes Stirling's approximation. By symmetry, the same conclusion can be drawn for qudit B (with M replaced by P). The curious observation to make here is that in the odd case, which enables a protocol for NOON state production, the pre-measurement entanglement within the qudits is *less* than that for the even case. While number-parity effects are ubiquitous in fermionic systems [32–36], they are less frequently encountered in bosonic models. The situation reported here displays some features in common with the work of [37].

Heisenberg-limited interferometry.— Finally, we establish that the system is capable of interferometry with sensitivity at the Heisenberg limit, through the archetypal example of parameter estimation through the phase of a NOON state [1, 3]. Consider initial state (4) with $N = M + P$ odd, and $\phi = 0$. A new phase φ is encoded into the bosons at site 4 through a transformation, $a_4^\dagger \mapsto \exp(i\varphi)a_4^\dagger$ (cf. [14]). This still corresponds to (4), but now with $\phi = P\varphi$, a phenomenon known as *phase super-resolution* [23, 24].

Again for time interval $t = t_m$, the imbalance between sites 1 and 3 is obtained from (5) as

$$\langle N_1 - N_3 \rangle = (-1)^{(N+1)/2} M \cos(P\varphi).$$

Fig. 3 shows the dependence of the fractional population $\langle N_1 - N_3 \rangle / M$ on parameters φ and the dimensionless time Jt .

Next, it can be confirmed that $\langle (N_1 - N_3)^2 \rangle = M^2$, so

$$\begin{aligned}\Delta \langle N_1 - N_3 \rangle &= \sqrt{\langle (N_1 - N_3)^2 \rangle - \langle N_1 - N_3 \rangle^2} \\ &= M |\sin(P\varphi)|.\end{aligned}$$

Using the standard estimation theory approach [1, 3], it is found that the system achieves Heisenberg-limited phase sensitivity since

$$\Delta\varphi = \frac{\Delta \langle N_1 - N_3 \rangle}{|d \langle N_1 - N_3 \rangle / d\varphi|} = \frac{1}{P}.$$

This is an improvement on the classical shot-noise case where $\Delta\varphi \sim 1/\sqrt{P}$ [1, 3].

Conclusion.— We have provided an example of integrable atomtronic interferometry, through an extended Bose-Hubbard model, with four sites arranged in a closed square. The integrable properties of the model furnished the necessary tools to understand the dynamics of the system in the resonant tunneling regime. It allowed for the analytic calculation of dynamical expectation values.

This, in turn, informed the relevant time interval required to implement certain measurement protocols. The probabilities for measurement outcomes were computed

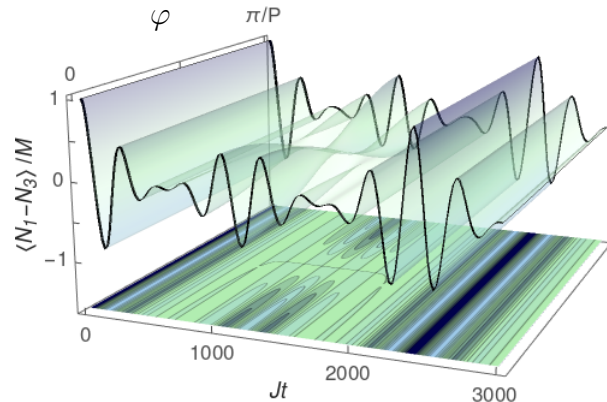


FIG. 3. Dependence of $\langle N_1 - N_3 \rangle / M$ as a function of dimensionless Jt and phase φ , for initial state (4) with $M = 15$, $P = 10$, $\phi = P\varphi$, and $U/J = 8$. Upper surface: The colors range from light to dark blue, indicating lower and higher values for the imbalance population. The green color represents the region where $\langle N_1 \rangle \approx \langle N_3 \rangle$. Lower plane: The effect on the system's dynamics is highlighted, specifically for the limiting cases $\varphi = 0$ and $\varphi = \pi/P$, where it is seen that there is a minimum-maximum inversion at $t_m \approx 1206.373/J$.

through the density matrix. We demonstrated proof of principle examples that the integrable system functions as an identifier of NOON states produced by a black box processor, and as a simulator of such a processor.

Our study highlights the quantum information connections of the model by detailing its function as a hybrid qudit system subjected to a controlled-phase gate operation. This description complements other qudit studies in photonic [38–40] and NMR [41] settings, which are attracting attention due to the promise of increasing quantum computational capacity. It is anticipated that our results, in an atomtronic framework, may be transferable to these and other contexts.

In future research, we will undertake studies involving other states which may be useful for metrological applications, such as coherent states and Dicke states. We will examine the evolution of these input states, and investigate the resulting generation of entanglement. Particular emphasis will be given to the understanding of multipartite entanglement generation, beyond the bipartite investigations reported here.

D.S.G. and K.W.W. were supported by CNPq (Conselho Nacional de Desenvolvimento Científico e Tecnológico), Brazil. A.F. acknowledges support from CNPq - Edital Universal 430827/2016-4. A.F. and J.L. received funding from the Australian Research Council through Discovery Project DP200101339. J.L. acknowledges the traditional owners of the land on which The University of Queensland is situated, the Turrbal and Jagera people.

- [1] L. Pezzé et al., Rev. Mod. Phys. **80**, 035005 (2018).
[2] K. Bongs, et al., Nature Reviews Physics **1**, 731 (2019).
[3] H. Lee, et al., J. Mod. Opt. **49**, 2325 (2002).
[4] C. Gross and I. Bloch, Science **357**, 995 (2017).
[5] R.A. Pepino et al., Phys. Rev. Lett. **103**, 140405 (2009).
[6] R. Dumke, et al., J. Opt. **18**, 093001 (2016).
[7] L. Amico, et al., New J. Phys. **19**, 020201 (2017).
[8] S Pandey, et al., Nature **570**, 205 (2019).
[9] M.K. Olsen and A.S. Bradley, Phys. Rev. A **91**, 043635 (2015).
[10] K. Wittmann Wilmann, et al., Commun. Phys. **1**, 91 (2018).
[11] T. Haug, et al., Phys. Rev. A **97**, 013633 (2018).
[12] J. Polo, et al., Phys. Rev. Lett. **123**, 195301 (2019).
[13] E. Compagno, et al., arXiv:191201092.
[14] T. Lahaye, et al., Phys. Rev. Lett. **104**, 170404 (2010).
[15] D. Poilblanc, et al., Europhys. Lett. **22**, 537 (1993).
[16] L.F. Santos and M. Rigol, Phys. Rev. E **81**, 036206 (2010).
[17] P. Calabrese, et al., J. Stat. Mech. 064001 (2016).
[18] T. Kinoshita, et al., Nature **440**, 900 (2006).
[19] J. Daboul, et al., J. Phys. A: Math. Gen. **36**, 2525 (2003).
[20] A. Muthukrishnan and C.R. Stroud Jr., Phys. Rev. A **62**, 052309 (2000).
[21] G.K. Brennen, et al., Phys. Rev. A **71**, 052318 (2005).
[22] G.J. Pryde and A.G. White, Phys. Rev. A **68**, 052315 (2003).
[23] M.W. Mitchell et al., Nature **429**, 161 (2004).
[24] K.J. Resch, et al., Phys. Rev. Lett. **98**, 223601 (2007).
[25] M.A. Baranov, Phys. Rep. **464**, 71 (2008).
[26] T. Lahaye et al., Rep. Prog. Phys. **72**, 126401 (2009).
[27] A.P. Tonel, et al., J. Phys. A: Math. Theor. **48**, 494001 (2015).
[28] A.P. Tonel, et al., SciPost Phys. Core **2**, 003 (2020).
[29] T.R. Bromley, et al., Phys. Rev. A **95**, 052313 (2017).
[30] W.H. Zurek, et al., Phys. Rev. Lett. **70**, 1187 (1993).
[31] F. Buscemi, et al., Phys. Rev. A **75**, 032301 (2007).
[32] K.A. Matveev and A.I. Larkin, Phys. Rev. Lett. **78**, 3749 (1997).
[33] G. Zürn, et al., Phys. Rev. Lett. **111**, 175302 (2013).
[34] S. Matsuo, et al., Sci. Rep. **5**, 11723 (2015).
[35] C. Schilling and R. Schilling, Phys. Rev. A **93**, 021601 (2016).
[36] E.T. Mannila, et al., Phys. Rev. B **100**, 020502(R) (2019).
[37] D. Agboola, et al., J. Phys. B: At. Mol. Opt. Phys. **51**, 14530 (2018).
[38] R.-B. Jin, et al., Quantum Sci. Technol. **1**, 015004 (2016).
[39] M. Kues, et al., Nature **546**, 622 (2017).
[40] P. Imany, et al., npj Quantum Inf. **5**, 59 (2019).
[41] A. Z. Khoury et al., Phys. Rev. A **97**, 042343 (2018).

APPENDIX

A. Energy bands and effective Hamiltonian

Here we give an overview of the origin for the effective Hamiltonian (2). Recall that the integrability condition is $U_{13} = U_{24} = U_0$ and $U_{12} = U_{23} = U_{34} = U_{14}$. When

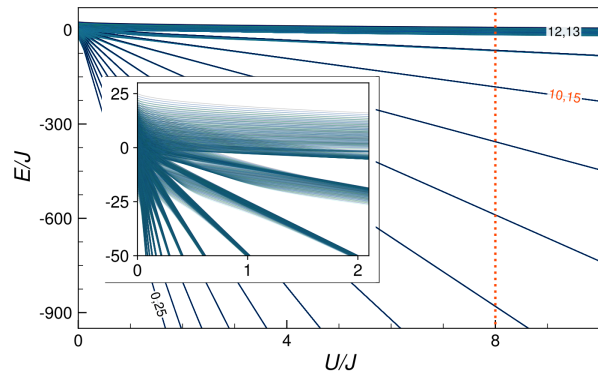


FIG. 4. Dimensionless energy eigenvalues E/J as a function of dimensionless coupling U/J , where $U = (U_{12} - U_0)/4$ and $C = 0$. Results are shown for $N = 25$, with M and P indicating the dependence of (9) in the $J \rightarrow 0$ limit. The orange vertical line is $U/J = 8$, for which quantum dynamics is described in Fig. 2, (except for the top left panel). The inset shows the large J limit, in which the bands begin to merge.

$J = 0$, the Fock state $|M - l, P - k, l, k\rangle$ is eigenstate of the Hamiltonian (1) with energy

$$E = C + \frac{U_0 - U_{12}}{4}(M - P)^2 \quad (9)$$

with $C = (U_0 + U_{12})N^2/4 - U_0/2$, independent of l and k , indicating degeneracies. For small values of J , the degeneracies are broken and lead to energy levels in well-defined bands, each with $2(M + 1)(P + 1)$ energy levels, except for N even, where the band with the highest energy, $M = P$, will have $(M + 1)(P + 1)$ levels. The level energy structure of the case we are analyzing, with $N = 25$, is shown in Fig. 4. In it, we highlight in red the band with $M = 15$ and $P = 10$ (and vice versa).

An effective Hamiltonian for each band is obtained by consideration of second-order processes. Associated to labels M and P , such that $N = M + P$, we obtain

$$\begin{aligned} H_{\text{eff}} = & \frac{J^2}{16U(M - P + 1)} \left(a_1 a_3^\dagger + a_3 a_1^\dagger \right) \left(a_2^\dagger a_2 + a_4^\dagger a_4 \right) \\ & + \frac{J^2}{16U(M - P + 1)} \left(a_1 a_1^\dagger + a_3 a_3^\dagger \right) \left(a_2^\dagger a_4 + a_4^\dagger a_2 \right) \\ & - \frac{J^2}{16U(M - P - 1)} \left(a_2 a_2^\dagger + a_4 a_4^\dagger \right) \left(a_1^\dagger a_3 + a_3^\dagger a_1 \right) \\ & - \frac{J^2}{16U(M - P - 1)} \left(a_2 a_4^\dagger + a_4 a_2^\dagger \right) \left(a_1^\dagger a_1 + a_3^\dagger a_3 \right) \\ & + \frac{J^2}{16U} \left(\frac{1}{M - P + 1} - \frac{1}{M - P - 1} \right) \\ & \times \left(a_1^\dagger a_2 a_3 a_4^\dagger + a_1^\dagger a_2^\dagger a_3 a_4 + a_1 a_2^\dagger a_3^\dagger a_4 + a_1 a_2 a_3^\dagger a_4^\dagger \right). \end{aligned}$$

This expression is equivalent to (2), up to a constant.

B. Non-destructive measurement

Here we show that the measurement protocol for NOON state identification using the effective Hamiltonian (2) is non-destructive with respect to qudit B. To establish this, it suffices to show that at measurement time t_m there is no entanglement between the qudits, such that a measurement performed on qudit A does not cause wavefunction collapse for qudit B.

From (4) define $|\Lambda(t, \phi)\rangle = \exp(-itH_{\text{eff}}) |\Phi(\phi)\rangle$. Generalizing Eq. (8) it is found that (recall N is chosen to be odd)

$$\begin{aligned} |\Lambda(t_m, 0)\rangle &= \frac{K(N+1, 0)}{2\sqrt{2}} (|M, P, 0, 0\rangle + |M, 0, 0, P\rangle) \\ &\quad + \frac{K(N-1, 0)}{2\sqrt{2}} (|0, 0, M, P\rangle + |0, P, M, 0\rangle), \\ |\Lambda(t_m, \pi)\rangle &= \frac{K(N+1, \pi)}{2\sqrt{2}} (|M, P, 0, 0\rangle - |M, 0, 0, P\rangle) \\ &\quad + \frac{K(N-1, \pi)}{2\sqrt{2}} (|0, 0, M, P\rangle - |0, P, M, 0\rangle) \end{aligned}$$

where $K(m, \phi) = (-1)^{m/2} + \exp(i\phi)$. Note that one of $K(N+1, \phi)$ and $K(N-1, \phi)$ is necessarily zero for N odd and $\phi = 0, \pi$.

It is recognized from the above equations that the possible measurements of the number of particles at site 3 are either 0 or M , and always occur with probability 1. Moreover, the post-measurement state of qudit B is a NOON state with the same symmetry or antisymmetric as the input NOON state for qudit B. That is, the identification of the NOON state loaded into qudit B is achieved without destruction of the NOON state.

C. Probabilities and fidelities

Here we provide benchmarks establishing the effectiveness of Hamiltonian (1) in the simulation of the black box processor \mathcal{P} , through numerical calculation of probabilities and outcome fidelities. A general N -particle state can be expressed as

$$|\Theta\rangle = \sum_{j,k,l=0}^N c_{j,k,l} |j, k, l, N-j-k-l\rangle$$

such that $c_{j,k,l} = 0$ if $j+k+l > N$, and $\sum_{j,k,l=0}^N |c_{j,k,l}|^2 = 1$.

When a measurement is made at site 3, the probability $\mathcal{P}(r)$ to obtain the measurement outcome r is

$$\mathcal{P}(r) = \sum_{j,k=0}^N |c_{j,k,r}|^2 \quad (10)$$

satisfying $\sum_{r=0}^N \mathcal{P}(r) = 1$. After the measurement, the wavefunction collapses to

$$|\Theta(r)\rangle = \frac{1}{\sqrt{\mathcal{P}(r)}} \sum_{j,k=0}^N c_{j,k,r} |j, k, r, N-j-k-r\rangle$$

such that $\langle \Theta(r) | \Theta(r) \rangle = 1$. Set

$$|\Phi(r, \phi)\rangle = \frac{1}{\sqrt{2}} |M-r, P, r, 0\rangle + \frac{\exp(i\phi)}{\sqrt{2}} |M-r, 0, r, P\rangle$$

and define the outcome fidelity $\mathcal{F}(r, \phi)$ to be

$$\mathcal{F}(r, \phi) = |\langle \Phi(r, \phi) | \Theta(r) \rangle|. \quad (11)$$

We take $|\Theta\rangle = \exp(-it_m H) |15, 10, 0, 0\rangle$ and use (1) with $U/J = 8$ to numerically calculate the measurement probabilities and outcome fidelities through (10,11). The results are given below in Table 1.

Measurement	Probability	Phase	Fidelity
r	$\mathcal{P}(r)$	ϕ	$\mathcal{F}(r, \phi)$
15	0.493898	0	0.999593
14	0.002814	0	0.600630
13	0.000237	0	0.515582
12	0.000149	0	0.070958
11	0.000311	0	0.023097
10	0.001182	0	0.002501
9	0.000252	0	0.007847
8	0.000235	0	0.011905
7	0.000231	π	0.014797
6	0.000254	π	0.010138
5	0.000168	π	0.022435
4	0.000176	π	0.026081
3	0.000144	π	0.057712
2	0.000291	π	0.449405
1	0.001398	π	0.839876
0	0.497463	π	0.996048

TABLE I. Measurement probabilities and fidelities after evolution under (1) until time t_m . The initial state is $|15, 10, 0, 0\rangle$, and $U/J = 8$ as used in Figs. 2, 3, 4. The calculations show that the highest fidelity outcomes, close to 1, occur with the highest probabilities, close to 1/2. This is in agreement with the results predicted by the effective Hamiltonian (2).